5-2023

Petrogenetic history of lava flows from the Casitas Shield in the Southern Volcanic Zone, Chile

Maeve S. Mikulski
Bates College, mmikulsk@bates.edu

Petrogenetic history of lava flows from the Casitas Shield in the Southern Volcanic Zone, Chile

A Senior Thesis

Presented to

The Faculty of the Department of Earth and Climate Sciences

Bates College

In partial fulfillment of the requirements for the

Degree of Bachelor of Science

By

Maeve S. Mikulski

Lewiston, Maine

April 20, 2023

Acknowledgements

I would like to thank the Bates College department of Earth and Climate Sciences; thank you to my professors, my classmates, and my fellow TAs, for the hard work they have put in to make the various multi-day field trips and gloomy Carnegie basement labs as fun and welcoming as possible. It has been a pleasure to be a part of this department and to watch it continually grow with the world around it.

I would like to specifically thank Mark Lessard for his guidance in the use of the SEM and all things microscopy – thanks for helping me finally get my hands on some data and grab some pretty pictures along the way. To Dyk Eusden, thank you for helping me grow in my love for fieldwork during the time we overlapped at Bates. I owe a lot of my confidence in my work and my ideas to you.

I would especially like to give a big thanks to my advisor, Andrew Wulff. Thank you for your endless hours of support and offers of blueberry crumb donuts. Working with this data would have been nowhere near as fun without the stories that went along with it.

To Bates Women's Rowing, you know I couldn't have done it without your support. There have been plenty of ups and downs, and you all have always been there ready to scream and cheer or help pick me up and dust me off, accordingly.

Finally, I would like to give a huge thank you to my family and friends for their love and support in everything I do. None of this would have been possible without being able to come home and rant to you guys.

Table of Contents

Acknowledgements ii

Table of Contents iii

Table of Figures iiv

Abstract v

1. Introduction 6

1.1 Geologic Background *6*

1.2 Petrogenetic Processes *8*

1.3 Study Area *11*

1.4 Objectives and Significance *12*

2. Methods 14

2.1 Sample Collection *14*

2.2 Petrographic Thin Section Analysis *14*

2.3 X-Ray Fluorescence *17*

3. Results 19

3.1 Major and Trace Element Geochemistry *19*

3.2 Zoned Plagioclase *23*

3.3 Temperatures of Formation *24*

4. Discussion 30

4.1 Eruptive Episodes *30*

4.2 Primitivity *31*

4.3 Crystallization Temperatures and Dominant Petrogenetic Processes *32*

5. Conclusion 36

References 37

Appendix 39

Table of Figures

Figure 1.1: Map of the Southern Volcanic Zone (Hickey-Vargas and Holbik, 2016) 6

Figure 1.2: Diagram of the MASH zone model (Winslow et al. 2016) 9

Figure 1.3: Map of the Descabezado Grande-Cerro Azul volcanic complex (Hildreth and Drake, 1992) 13

Figure 2.1: Map of sample locations 15

Figure 2.2: Example of stacked flows at Tatara-San Pedro 15

Figure 2.3: Petrographic thin section from flow CSS-11 16

Figure 2.4: Scanning electron microscope at Bates College 17

Figure 3.1: Rock type plotted by total alkalis vs. silica 19

Figure 3.2: Tholeiitic vs. Calc-Alkaline classification plot 20

Figure 3.3: Stratigraphic position plotted against MgO, Mg#, Sr, Ni, and Cr 21

Figure 3.4: Strontium vs. magnesium ploted with data from the whole subduction arc 22

Figure 3.5: Rubidium vs. magnesium ploted with data from the whole subduction arc 22

Figure 3.6: Normal zoning in plagioclase feldspar under SEM 23

Figure 3.7: Oscillatory zoning in plagioclase feldspar under SEM 23

Figure 3.8: Oscillatory zoning in plagioclase feldspar under SEM 24

Figure 3.9: Feldspar and olivine composition diagrams for CSS-1 25

Figure 3.10: Feldspar and olivine temperature of formation graph for CSS-1 25

Figure 3.11: Feldspar and olivine composition diagrams for CSS-5 26

Figure 3.12: Feldspar and olivine temperature of formation graph for CSS-5 27

Figure 3.13: Feldspar and olivine composition diagrams for CSS-10 28

Figure 3.14: Feldspar and olivine temperature of formation graph for CSS-10 28

Figure 3.15: Feldspar and olivine composition diagrams for CSS-11 29

Figure 3.16: Feldspar and olivine temperature of formation graph for CSS-11 29

Figure 4.1: Plot comparing strontium vs. silica for the entire subduction arc, the DGCA, and the TSP 35

Abstract

Relatively few studies have investigated the geochemistry of the Descabezado Grande-Cerro Azul (DGCA) volcanic complex, located in the Southern Volcanic Zone (SVZ) of the Chilean Andes. Lava samples were collected in stratigraphic order from vertical stacks of flows exposed along the walls of steep canyons incised in the flanks of the Casitas shield of Cerro Azul. In order to determine dominant petrogenetic processes and identify changes in the composition of the magmatic system over time, this project obtained mineral analyses using x-ray fluorescence (XRF) as well as textural analyses of petrographic thin sections using scanning electron microscopy (SEM). Analyses of the younger lavas were found to be composed mostly of basalts with some basaltic andesite compositions, results that are more primitive than older lavas previously sampled in this section and throughout the Southern Volcanic Zone.

1. Introduction

1.1 Geologic Background

The Andean Volcanic Belt is a continental volcanic arc formed by the subduction of the Nazca plate beneath the South American plate at a rate of around 7-9cm/yr (Stern 2004). The belt spans the entirety of the western coast of South America and is split into four compositionally distinct volcanic zones: the Northern Volcanic Zone, Central Volcanic Zone, Southern Volcanic Zone, and Austral Volcanic Zone, which are separated by gaps in volcanism that are the product of the flat slab subduction of the Nazca ridge (forming the Peru Gap) and the Juan Fernandez ridge (forming the Chile Gap).

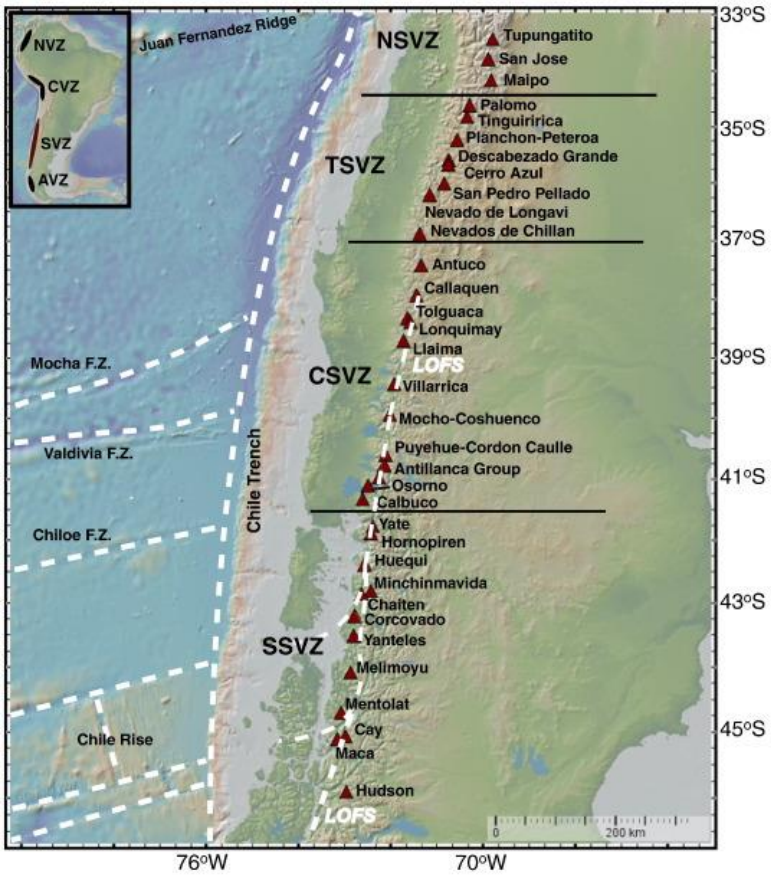

Figure 1.1: A map of the Southern Volcanic Zone depicting the different subdivisions. The locations of different fault zones in the Nazca plate and major stratovolcanoes in each zone are marked. (from Hickey-Vargas and Holbik 2016)

The Southern Volcanic Zone (SVZ) shown in Figure 1.1 is located between latitudes 33°S and 47°S and is further split into the Northern (NSVZ), Transitional (TSVZ), Central (CSVZ), and Southern (SSVZ) Southern Volcanic Zones. The continental crust is proposed to thicken northward through the entire SVZ, from 30km in the SSVZ to 60km in NSVZ. (Salas et al. 2017). Most of the volcanic centers in the SVZ are located between 270km to 285km from the Chile trench, indicating that the Nazca plate is subducting at a nearly constant angle throughout the subduction zone (Stern 2004).

Studies published (e.g. Hildreth and Moorbath, 1988) found that northward through the SVZ the geochemical evidence of crustal contamination also wanes, suggesting that the crust is thinning. Evidence includes southward decreasing K_2O and $^{87}Sr/^{86}Sr$ ratios (Hildreth and Moorbath, 1988). This study also identified a trend in magma compositions North of 37°S in the NSVZ and TSVZ demonstrating that stratovolcanoes are dominated by silicic magmatism, and it is rare to find any primitive basalts (Hildreth and Moorbath, 1988). The most primitive signatures measured have come from short lived, monogenetic cones that store and homogenize magma in the crust for long periods before eruption. (Winslow et al. 2020).

The Transitional Southern Volcanic Zone refers to the portion of the arc between 34.5° and 37°S and consists of Quaternary stratovolcanoes with compositions ranging from basaltic andesites to rhyolites (Hickey-Vargas and Holbik, 2016). Long lived volcanic systems that have been previously studied such as Planchon-Peteroa (Tormey et al. 1995) and Descabezado Grande-Cerro Azul (Hildreth and Drake, 1992) fit within the trend of a higher amount of crustal contribution than in the nearby CSVZ, however studies such as Dungan et al. 2001 found that in cases like at Tatara-San Pedro a much broader range in levels of primitivity. Dungan et al. 2001

suggests a need for the in-depth study of early and late stages in these systems with higher density sampling.

The similarities in composition of the subducting plate, subduction angle, distance from the trench, and gradual crustal thinning lead to the question of why the products of SVZ magmatic centers (even within those restricted to one segment such as the TSVZ) differ so dramatically. Hildreth and Moorbath (1988) suggested a model in which the upper plate, consisting of Jurassic and Cretaceous volcanic strata that form the Andean Cordillera, played a larger role and that MASH zones (Mixing, Assimilation, Storage, Homogenization) in the lower crust were responsible for changing the geochemical characteristics of subduction magmas during their ascent to the surface. MASH zones like the one depicted in Figure 1.2, accumulate new magmas from the overlying plate that then interact with arc magmas derived from the partial melting of the asthenosphere, and are typically located in areas with a crustal thickness of >50km. (Hildreth and Moorbath 1988; Winslow et al. 2016).

1.2 Petrogenetic Processes

Magmatic differentiation is the process by which a parental melt crystallizes to produce an igneous series (Philpotts and Ague, 2009). A parental magma is defined as the most primitive magma in a series from which more evolved compositions are derived. There are four main processes by which parental magmas may be modified: fractional crystallization, assimilation, partial melting, and magma mixing.

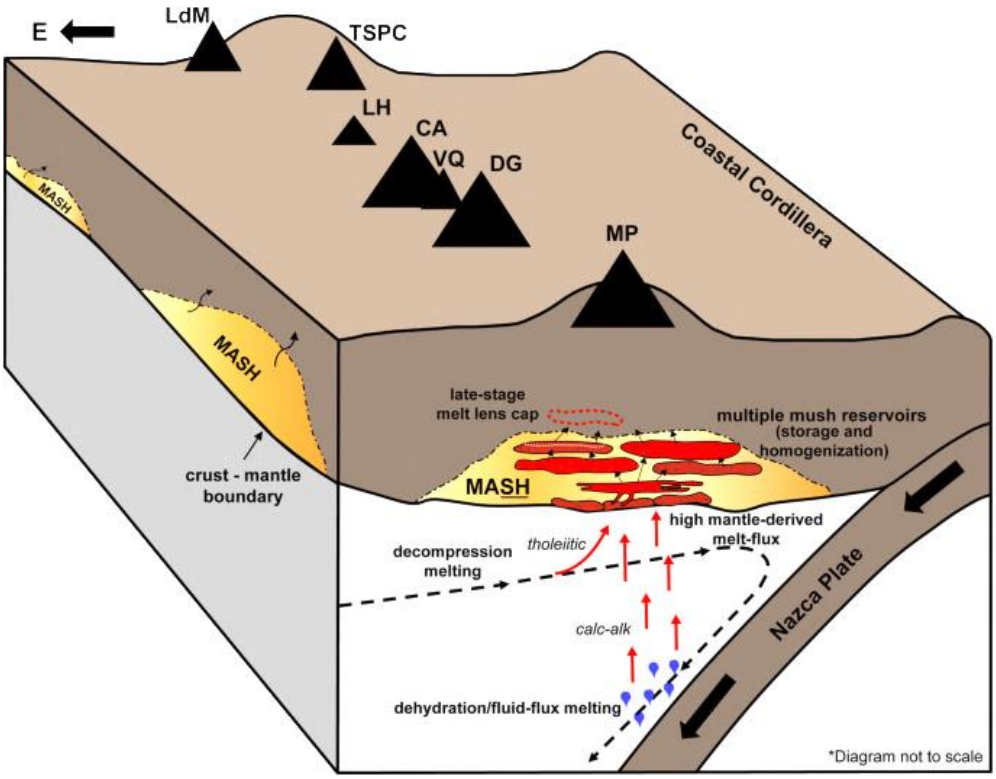

Figure 1.2: A diagram showing the possible MASH zone under Manantial Pelado, a stratocone North of the DGCA. The schematic shows the melt coming from the mantle being stored with the melt derived from the continental crust, before further interacting with the crust on ascent to the surface. From Winslow et al. 2016.

Fractional crystallization was a model of crystal-liquid differentiation first proposed in The Reaction Principle in Petrogenesis by Norman L. Bowen in 1922. Bowen's reaction series is the sequence of crystallization from a basaltic magma, with a depletion of magnesium and iron over time in mafic minerals and a depletion of calcium over time in felsic minerals. Overall, Bowen found that a magma undergoing fractional crystallization becomes richer in silica over time. As early-forming minerals such as olivine and plagioclase are fractionated and the temperature of the magma decreases, the overall composition of the melt changes and different minerals begin to form such as pyroxenes and albite. Evidence of this fractionation can be seen in thin section through the presence of normal zoning in a mineral like olivine or plagioclase. Early formed minerals first form through homogenous nucleation within the magma and as the composition of

the melt changes around it, new rims form with higher ratios of other slightly less compatible elements. Olivine, for example, follows a similar trend, with higher ratios of iron to magnesium towards the outer edges of the compositionally zoned minerals.

The process of fractional crystallization has long been considered the only method by which a melt could differentiate. Bowen's model, however, does not consider the interaction of a magma with the country rock that it encounters within eruptive conduits or on the walls of the magma chamber. Pieces of country rock that fall into a magma and become assimilated within a melt can change the composition of the overall magma. Pieces of country rock that do not become assimilated are retained within the magma as xenoliths. This changed composition can then undergo fractional crystallization, producing different composition minerals than from the original magma. This process is considered to be assimilation-fractional crystallization (AFC). Evidence of assimilation can be seen in changes in mineral compositions and in whole rock geochemistry. Contact with country rock such as along the walls of conduits or magma chambers can cause partial melting, which also alters the composition of the magma. During partial melting, incompatible elements that are not easily incorporated into crystal structures due to a high charge (high field strength elements, HFSEs) or large ionic radius (large ion lithophile elements, LILEs) are added to the magma (Philpotts and Ague, 2009). Concentrations of these trace elements are used to describe the amount of crustal contribution and interaction a magma had during ascent or storage.

Magma mixing describes the process of contact between two magmas, which could be due to successive pulses of melt being added into a magmatic system. These magmas could be derived from the same source and have similar compositions or come from different sources and mingle until an intermediate composition between the two endmembers is formed (Philpotts and Ague,

2009). Evidence of this can be seen in oscillatory or reverse zoning of plagioclase feldspars, where a feldspar undergoing normal zoning suddenly begins to produce rims with a more calcic ratio after producing sodic rims or begins with a sodic core and becomes more calcic with each consequent rim. Mixing and homogenization is more likely to occur when two magmas are both highly liquid and have similarly low degrees of crystallization. If there is too great of a difference the magma compositions will not mix and instead form structures such as pillows that sink to the bottom of the magma chamber. Magma mixing is the petrogenetic process that dominates subduction arcs, due to new melt from the subducting plate rising and mixing with magmas present in the existing volcanic arc.

1.3 Study area

The Descabezado Grande-Cerro Azul (DGCA) volcanic complex lies within the Transitional Southern Volcanic Zone and consists of two Holocene stratovolcanoes (for which it is named) surrounded by over 12 vents and cinder cones. (Hildreth and Drake, 1992). The 20x30km volcanic field, depicted in Figure 1.3, sits on top of a 7Ma granodiorite pluton and the 0.3 Ma Casitas basaltic shield. (Winslow 2018; Drake, unpubl.). The Casitas Shield is formed by stacks of flows exposed in glacially carved valleys on the flanks of Cerro Azul. These flows flattened the topography of the area into a plateau and were deposited on tilted Mesozoic marine sediments and the Invernada Pluton (Hildreth and Drake, 1992). After the period in which the Casitas Shield was deposited, the behavior of the system changed from effusive vents into an edifice building stage with the alternating secular dominance of different vents. The flows of the Casitas Shield have not been characterized before and cannot be directly compared to the current compositions produced in the DGCA due to the separation in time and magma behavior, however they are important in understanding how the modern complex evolved.

While the current system was constructed throughout the late Pleistocene to early Holocene, the most recent volcanic activity from the Quizapu vent of Cerro Azul was responsible for two of South America's largest explosive eruptions in 1846-7 and 1932. (Winslow 2018; Hildreth and Drake, 1992; Higgins et al. 2015). The products from the modern active period of this complex volcanic system range from basaltic andesites to rhyolite with the Quizapu vent having erupted a range of compositions between 52-72% SiO2 during one eruption. (Hildreth and Drake, 1992). The more silicic stratovolcanoes and vents are located at the center of the complex while younger, more mafic monogenetic cones are located towards the western perimeter of the field, which can be seen in Figure 1.3. (Salas et al. 2017).

1.4 Objectives and significance

Relatively few studies have been done regarding the geochemistry of the Descabezado Grande-Cerro Azul volcanic complex. Studying the historic behavior of this magmatic system can lead us to a fuller understanding of the evolution of large volcanic complexes. The same system that formed the Quizapu vent, responsible for two of South America's largest eruptions, first formed the Casitas Shield which flattened out the topography before one vent began to dominate and the eruption style of the complex completely changed.

This study aims to use mineral and textural analyses of lava flows sampled stratigraphically from the Casitas shield underlying the DGCA in order to understand the petrogenetic history. This history can be used to determine flow temperatures and change in the composition of the magma chamber over time. This data can be used to put together a greater understanding of the entire volcanic complex and provide further insights into the behavior of the volcanic activity of the Transitional Southern Volcanic Zone or other continental convergent arc systems.

Figure 1.3: A map of the Descabezado Grande-Cerro Azul volcanic complex, with craters and vents marked by a triangle or hatched circle. Many of the mafic cones and vents such as Los Hornitos, Manantial Pelado, and La Resolana craters are located on the western edge of the field. From Hildreth and Drake, 1992.

2. Methods

2.1 Sample Collection

Samples for analysis were collected during a traverse across the Casitas Ridge by Dr. Andrew Wulff, which can be seen in Figure 2.1. Flows were sampled stratigraphically from stacks of flows like those in Figure 2.2. using stratigraphic position as a proxy for relative age during analysis. The lowest flows sampled were categorized as the Casitas Shield North (CSN) series, while the next series above it was categorized as Casitas Shield South (CSS). In this study upper CSS refers to the top 11 flows of the Casitas Shield South, as they are the stratigraphically highest and youngest flows sampled. Some rock samples were collected at intervals from the same laterally continuous flow to act as standards when comparing the same stratigraphic sequences in different locations. Samples were taken from the massive center of the flow to avoid contamination from the top or bottom of the flow and were trimmed in the field to remove any weathering. The samples were bagged to avoid further contamination and labeled for future analysis.

2.2 Petrographic Thin Section Analysis

Five of the collected rock samples were cut into thin sections. Thin sections are produced by first cutting samples into blocks using a Diamond Pacific TR-18 Slab Saw and then are further cut using a Lortone Inc Lapidary Trim Saw Model FS2. This process trims off the exterior of each sample that may have been contaminated and cuts each sample into an appropriate size before being sent to a commercial thin section cutting company to be made into petrographic thin sections with a thickness of 30μm and mounted on glass slides. The resulting thin sections were then polished for analysis.

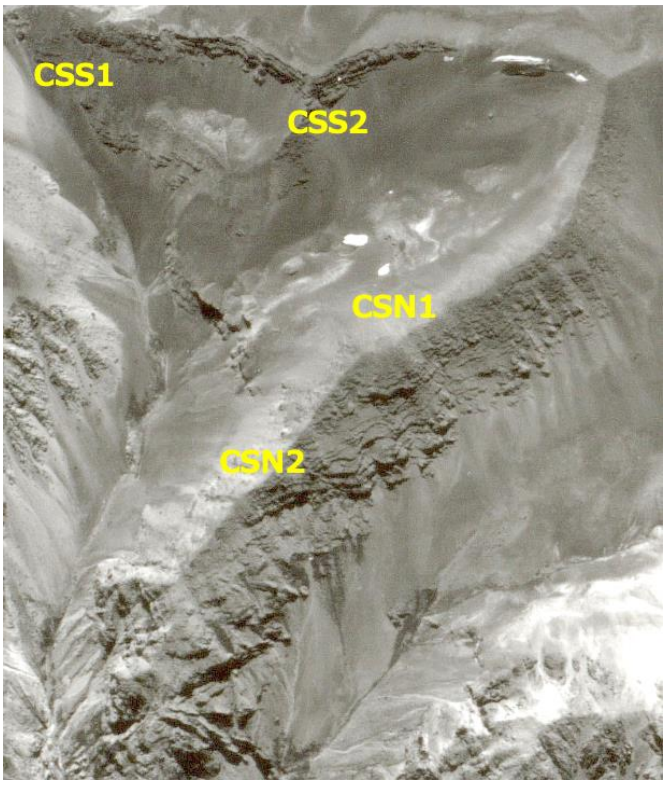

Figure 2.1 Sample sites on the Casitas Shield. Lateral continuity was confirmed by following common flows between each section.

Figure 2.2 An example of a stack of flows like the ones analyzed in this study. These flows are from Tatara-San Pedro, a volcano located to the North of the DGCA.

Thin sections, like the photomicrograph in Figure 2.3, were examined using an Olympus BH-2 Polarizing Microscope model BHSP at Bates College in plane- and cross-polarized light at all magnifications. The samples were also analyzed using the scanning electron microscope and energy dispersive spectrometer (SEM-EDS) located at Bates College (Figure 2.4). Thin sections were sputter coated with carbon with a Denton Vacuum DV1 Carbon Evaporation unit in order to ensure that no electron charging would interfere with the observation in the SEM. Samples were observed in the SEM at a magnification between 100-1000x. Semi-quantitative chemical analyses were performed using the EDS, which directs a beam of electrons at a chosen spot on the mineral, displacing inner shell electrons. Outer shell electrons then fill these open spaces in the inner shell, losing energy in the form of characteristic x-rays that are measured and used to identify the elements present in a mineral. These elements are given in major oxide percent and can be used alongside a mineral formula calculating program in order to determine the mineral being analyzed. These mineral assemblages can be compared to their solid solution diagrams to find the temperature of crystallization of each composition.

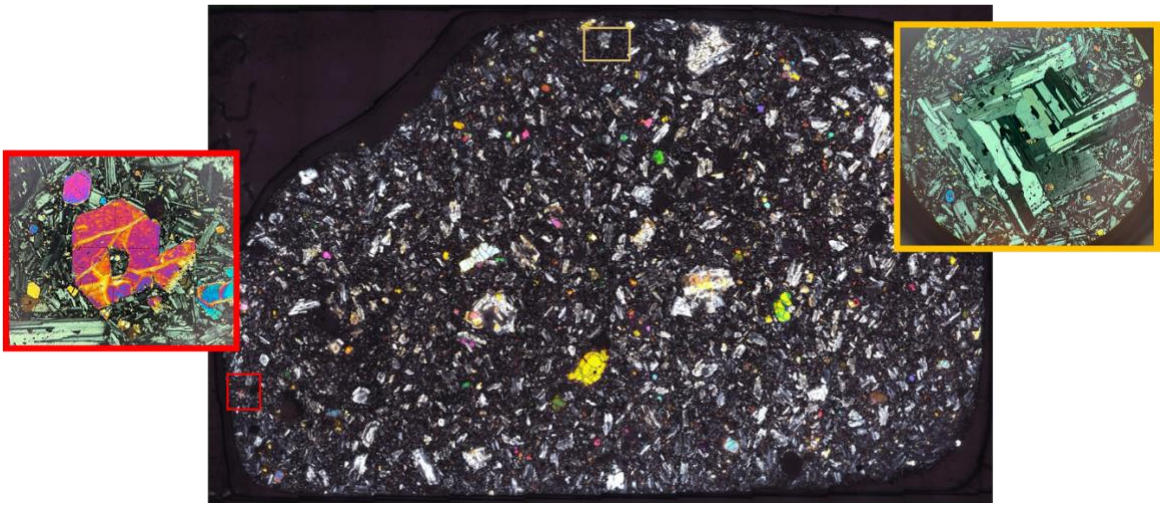

Figure 2.3 A petrographic thin section of CSS-11 shown in cross polarized light. Shown in red is a skeletal olivine and in yellow is a plagioclase feldspar.

Figure 2.4 The SEM-EDS located at Bates College where thin section samples were analyzed.

2.3 X-Ray Fluorescence

Similar to the EDS, the x-ray fluorescence spectrometer (XRF) analyzes the chemical composition of samples by measuring the released characteristic x-rays. Instead of being hit by a beam of electrons, the sample is struck with a spectrum of x-rays produced by an x-ray tube within the machine in order to dislodge inner shell electrons.

To prepare samples for XRF analysis, portions of the collected whole rock sample were crushed into a powder in an aluminum shatter box to a grain size of around 75 microns. The powdered samples were weighed and placed in platinum crucibles before being fired to 1050ºC to melt the samples and form uniform glass disks. Samples were sent to the Ronald B. Gilmore laboratory at the University of Massachusetts – Amherst and the XRF laboratory at Michigan State University where they were analyzed using a Siemens MRS-400 multi-channel

simultaneous X-ray spectrometer and a Bruker S4 PIONEER, respectively. Data from the XRF analysis of these samples was then plotted using the geochemical modeling software, IgPet, to compare the major and trace element trends of samples across the stratigraphy.

3. Results

3.1 Major and Trace Element Geochemistry

X-ray fluorescence data (see Appendix) from samples of each flow making up the CSS and CSN suite of lavas were plotted by total alkalis and silica and separated by rock type according to Cox-Bell-Pankhurst 1979 (Figure 3.1). The suite ranges through three different igneous rock types; andesite, basaltic andesite, and basalt. The CSN flows had a higher SiO_2 and total alkalis than the CSS flows and were split between andesites and basaltic andesites. The CSS flows were almost entirely basaltic andesites, with one plotting as a basalt. The sampled basalt dikes and tephra had some of the most mafic compositions.

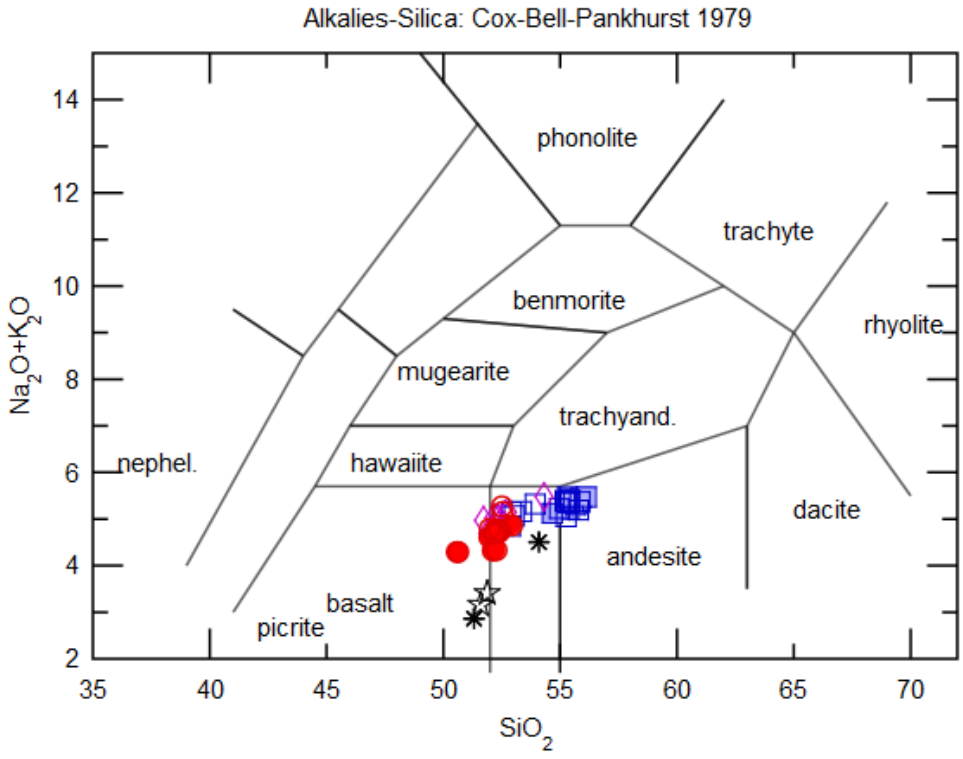

Figure 3.1 Rock type based on total alkali data, with samples from the higher, younger sections (CSS-1 through CSS-11) represented in red and the lower stratigraphy represented in blue and pink. Black stars and asterisks represent dikes and tephra. The suite trends towards more mafic compositions in the younger flows.

The suite was also plotted by FeO*/MgO against silica in Figure 3.2, separating the flows by calc-alkaline or tholeiitic affinities. The lowest CSN flows fall entirely within the calc-alkaline portion of the graph with the upper flows of the CSN series separating into calc-alkaline and tholeiitic. CSS-10 and CSS-11 are tholeiitic while the rest of the upper CSS series behave like calc-alkaline compositions but are still distinct from the lower CSS flows.

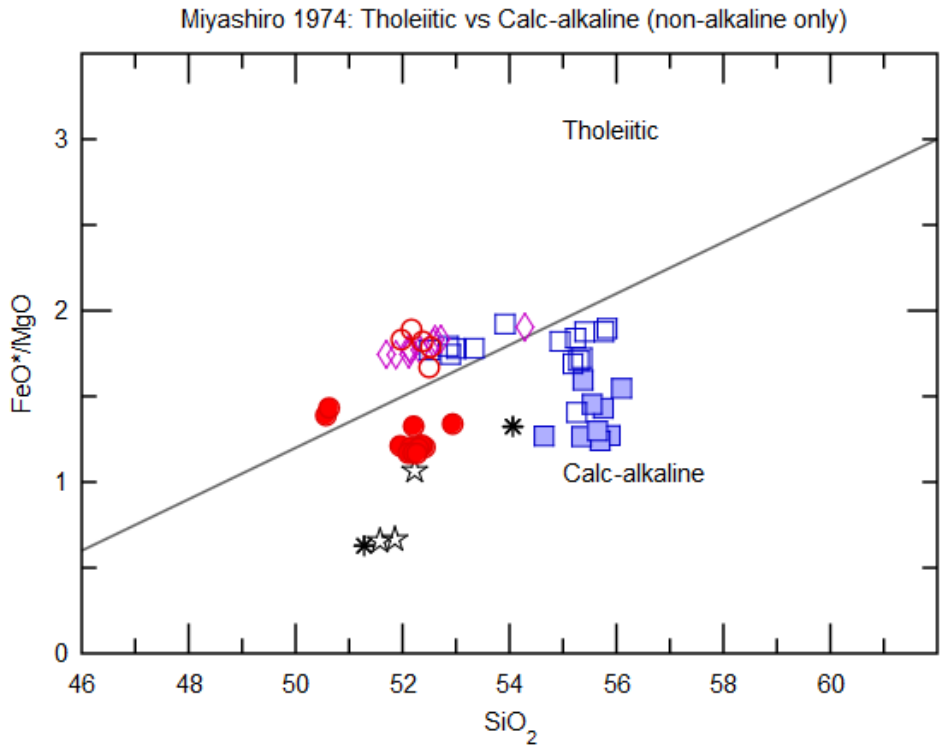

Figure 3.2 Classifying of the CSS-CSN series of flows as tholeiitic or calc-alkaline basalts. CSS-1 through CSS-11 are represented as red filled in circles and the lowest sampled flows from CSN are represented by blue squares.

The samples taken from the CSN-CSS suite were then plotted according to stratigraphy against several major and trace element compositions to compare the behavior of the different flows over time (Figure 3.3). CSS-1 through CSS-11 had a significantly higher magnesium and magnesium number than the lower stratigraphy. CSS-10 and CSS-11 have a lower content of both MgO and Mg# than the rest of the upper CSS flows. The CSN flows decrease in magnesium and magnesium number over time, while the compositions of the rest of the flows stay relatively

stable. The entire system decreases in strontium over time, with individual increases in the lower CSN series and the upper CSS series. The lower CSN series decreases in nickel, while the higher flows have a steady, low amount until the upper CSS series. The top 10 flows of the CSS have the highest nickel out of the whole suite. The same trends present with nickel are shown again with chromium.

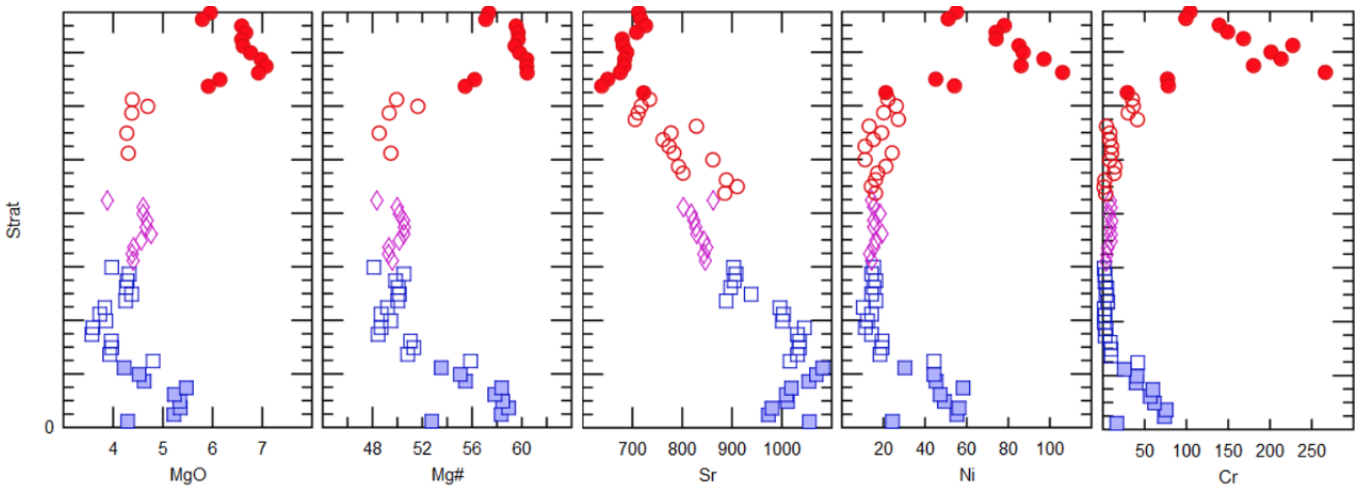

Figure 3.3 Compositional major and trace element data separated by stratigraphic position. MgO, Mg#, Sr, Ni, and Cr are depicted as indicators of melt composition primitivity.

The CSN-CSS suite was plotted alongside all published igneous composition data from the entirety of the Southern Volcanic Zone. In Figure 3.4, the entire CSN-CSS series has a higher strontium content than much of the rest of the SVZ. The upper CSS series also plots among the highest magnesium content of the SVZ. Figure 3.5 plots rubidium against magnesium, with the CSN-CSS suite being depleted in rubidium compared to the rest of the volcanic arc.

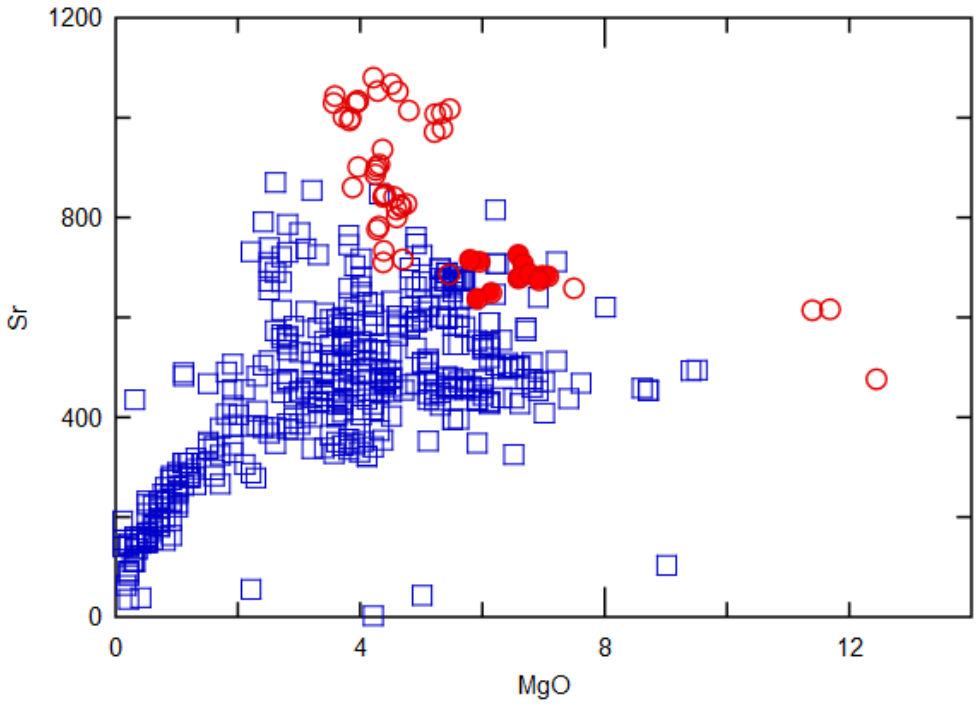

Figure 3.4 Strontium and MgO data from every volcanic center in the SVZ. The CSS-CSN series is plotted as red circles, with CSS-1 through CSS-11 represented by filled in red circles.

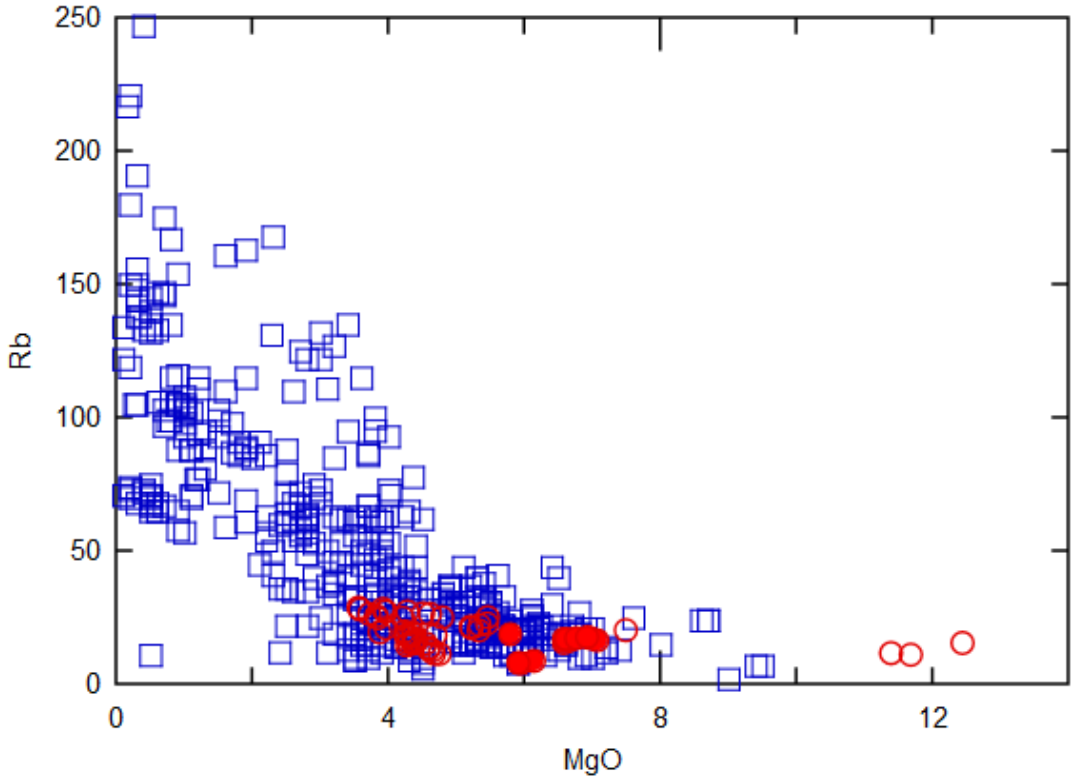

Figure 3.5 Rubidium and MgO data from every volcanic center in the SVZ. The CSS-CSN series is plotted as red circles, with CSS-1 through CSS-11 represented by filled in red circles.

3.2 Zoned Plagioclase

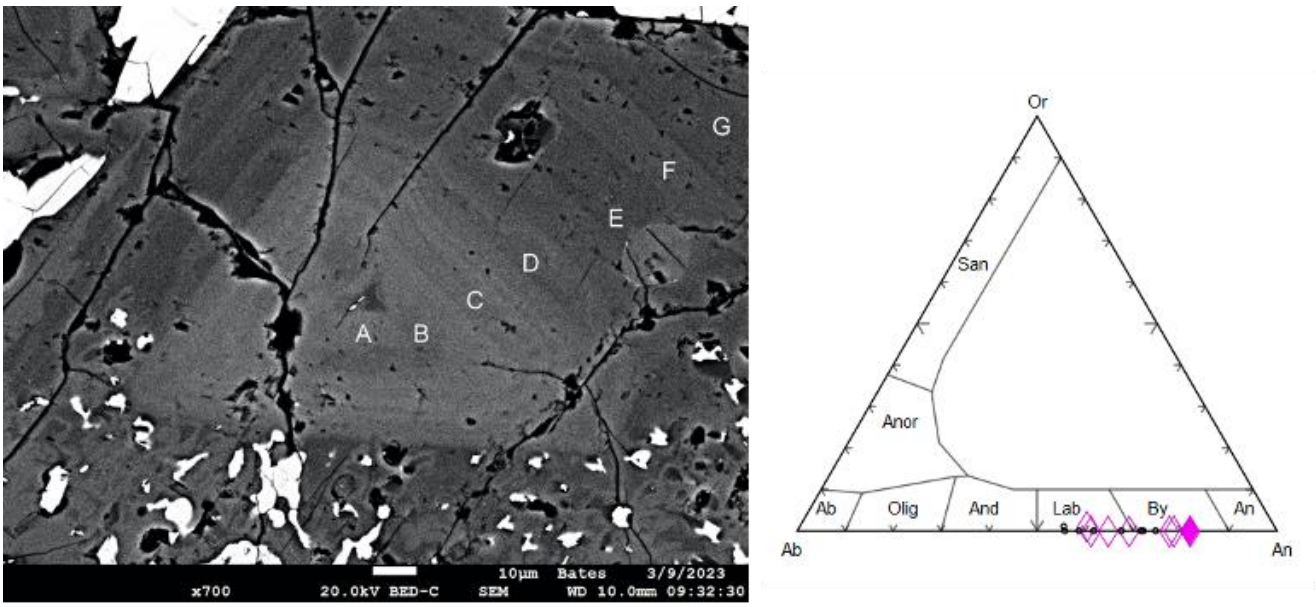

Figure 3.6 A zoned plagioclase feldspar from CSS-11 showing normal zoning from a calcic core to a sodic rim, with compositions plotted on a feldspar triangle. The core is shown with a filled in diamond, with each subsequent ring being an empty diamond.

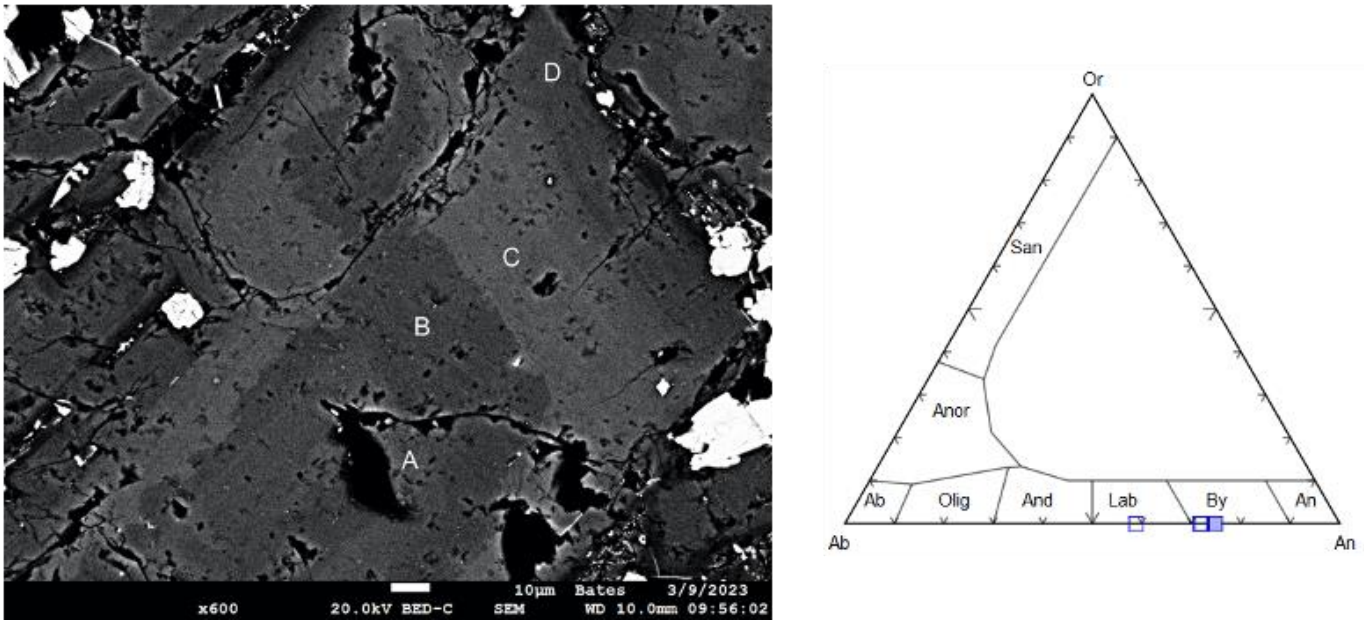

Figure 3.7 A zoned plagioclase feldspar from CSS-11 showing oscillatory zoning, with compositions plotted on a feldspar triangle. The core is shown with a filled in square.

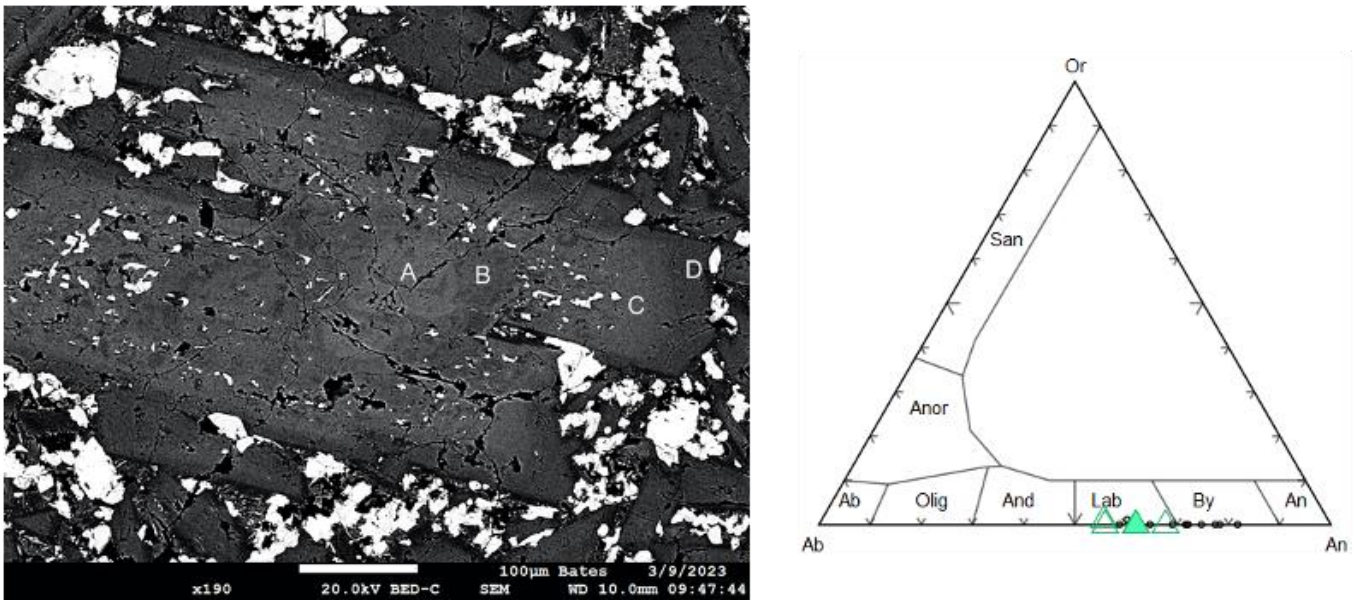

Figure 3.8 A zoned plagioclase feldspar from CSS-11 showing oscillatory zoning, with compositions plotted on a feldspar triangle. The core is shown with a filled in triangle.

Compositional zoning in plagioclase was only observed in petrographic thin sections from CSS-10 and CSS-11. Zoning was normal to oscillatory, with no examples of reverse zoning found. The normal zoning shown in Figure 3.6 has a core with six rims that get progressively more calcic. The oscillatory zoning in Figures 3.7 and 3.8 began with a sodic core and moved to a calcic rim, before moving back to a more sodic composition.

3.3 Temperatures of Formation

3.3.1 CSS-1

The compositions of ten plagioclase feldspars were taken and plotted on a ternary feldspar diagram (Figure 3.9). These feldspars showed compositions of $An_{56}Ab_{44}$ to $An_{71}Ab_{29}$. Four olivine compositions were plotted on a pyroxene olivine quadrangle and showed compositions between Fo_{54} to Fo_{72} (Figure 3.9). In Figure 3.10 these compositions were used to plot the average temperatures of formation of the feldspars and olivines. The feldspars plotted

formation temperatures between 1310°C to 1375°C and the olivines plotted temperatures between 1360°C to 1500°C.

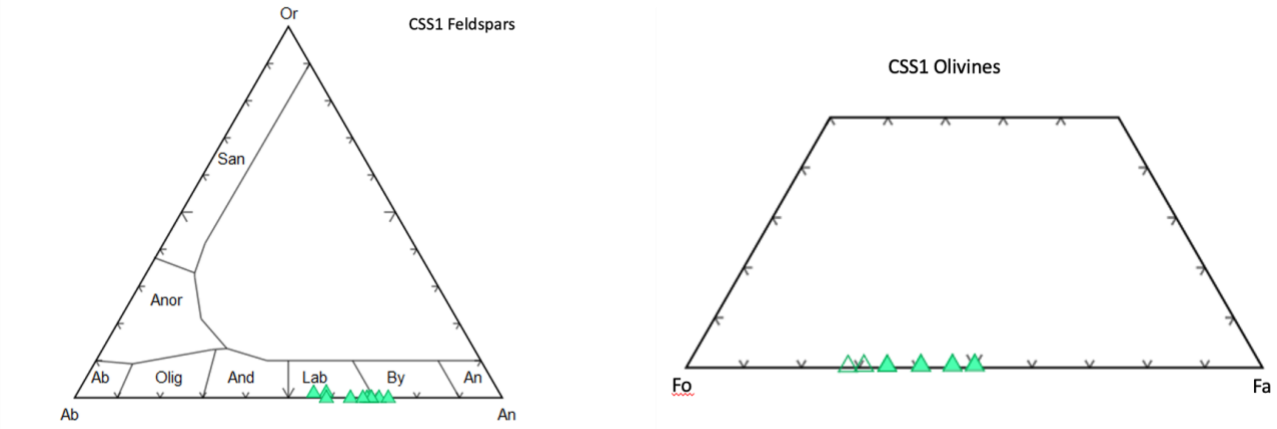

Figure 3.9 Left: Feldspar diagram with compositions from CSS-1. Cores are plotted as solid triangles and rims are plotted as plotted as empty triangles. Right: Olivine-pyroxene quad with compositions from CSS-1. Cores are plotted as solid triangles and rims are plotted as plotted as empty triangles.

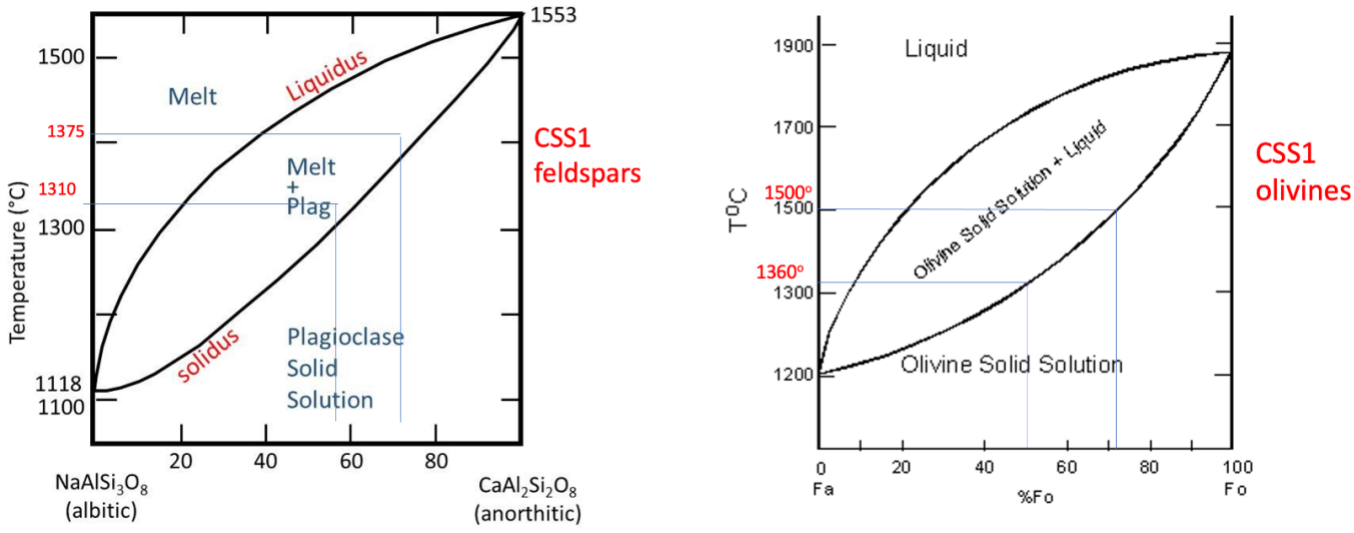

Figure 3.10 Left: A diagram of plagioclase feldspar solid solution with the end member compositions from CSS-1 plotted with their accompanying temperatures of formation. Right: A diagram of olivine solid solution with the CSS-1 compositions plotted showing the attributed temperatures of formation.

3.3.2 CSS-5

The compositions of eleven plagioclase feldspars were taken and plotted on a ternary feldspar diagram (Figure 3.11). These feldspars showed compositions of $An_{63}Ab_{37}$ to $An_{71}Ab_{29}$. One zoned olivine composition was plotted on a pyroxene olivine quadrangle and showed compositions between Fo_{57} to Fo_{69} (Figure 3.11). In Figure 3.12 these compositions were used to plot the average temperatures of formation of the feldspars and olivines. The feldspars plotted formation temperatures between 1300°C to 1375°C and the olivine data plotted temperatures around 1475°C.

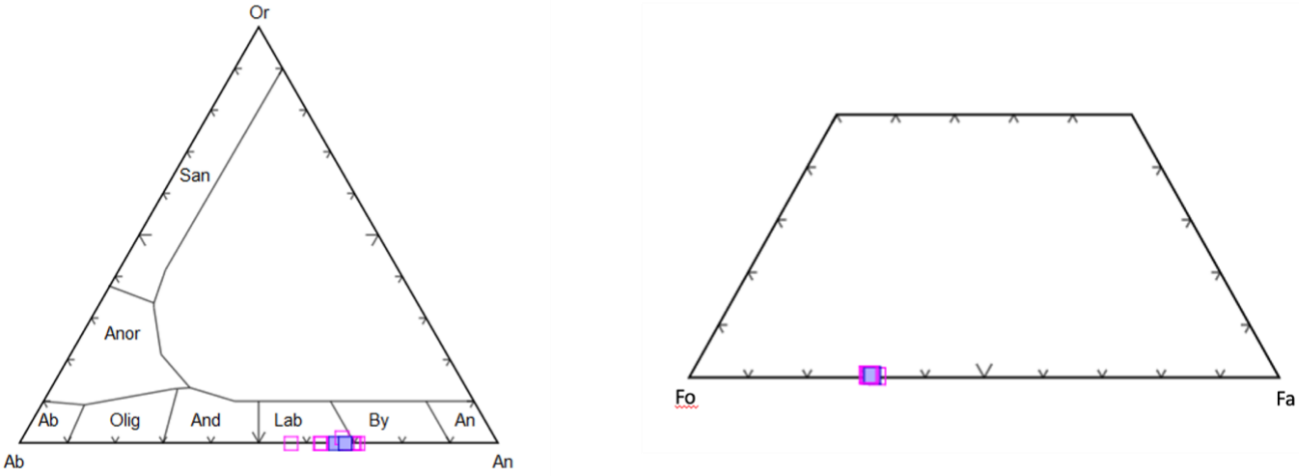

Figure 3.11 Left: Feldspar diagram with compositions from CSS-5. Cores are plotted as solid squares and rims are plotted as plotted as empty squares. Right: Olivine-pyroxene quad with compositions from CSS-5. Cores are plotted as solid squares and rims are plotted as plotted as empty squares.

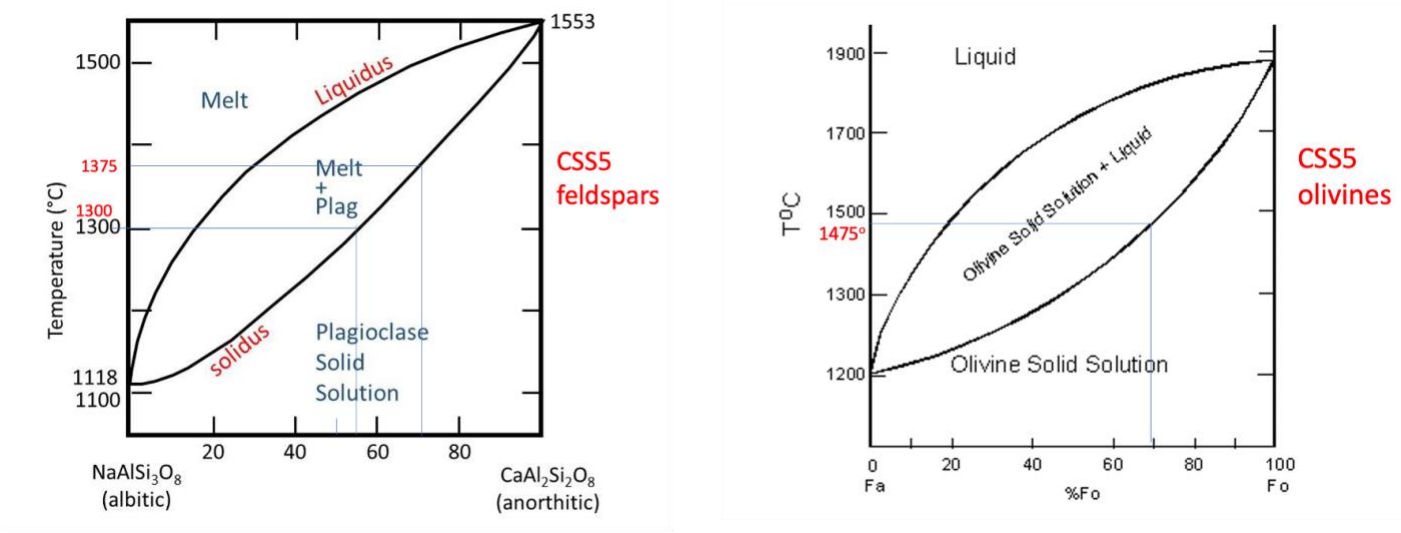

Figure 3.12 Left: A diagram of plagioclase feldspar solid solution with the end member compositions from CSS-5 plotted with their accompanying temperatures of formation. Right: A diagram of olivine solid solution with the CSS-5 compositions plotted showing the attributed temperatures of formation.

3.3.3 CSS-10

The compositions of five zoned plagioclase feldspars were taken and plotted on a ternary feldspar diagram (Figure 3.13). These feldspars showed compositions of $An_{43}Ab_{54}Or_4$ to $An_{84}Ab_{29}$. Seven olivine compositions were plotted on a pyroxene olivine quadrangle and showed compositions between Fo_{44} to Fo_{70} (Figure 3.13). In Figure 3.14 these compositions were used to plot the average temperatures of formation of the feldspars and olivines. The feldspars plotted formation temperatures between 1245°C to 1450°C and the olivines plotted temperatures around 1300°C to 1480°C.

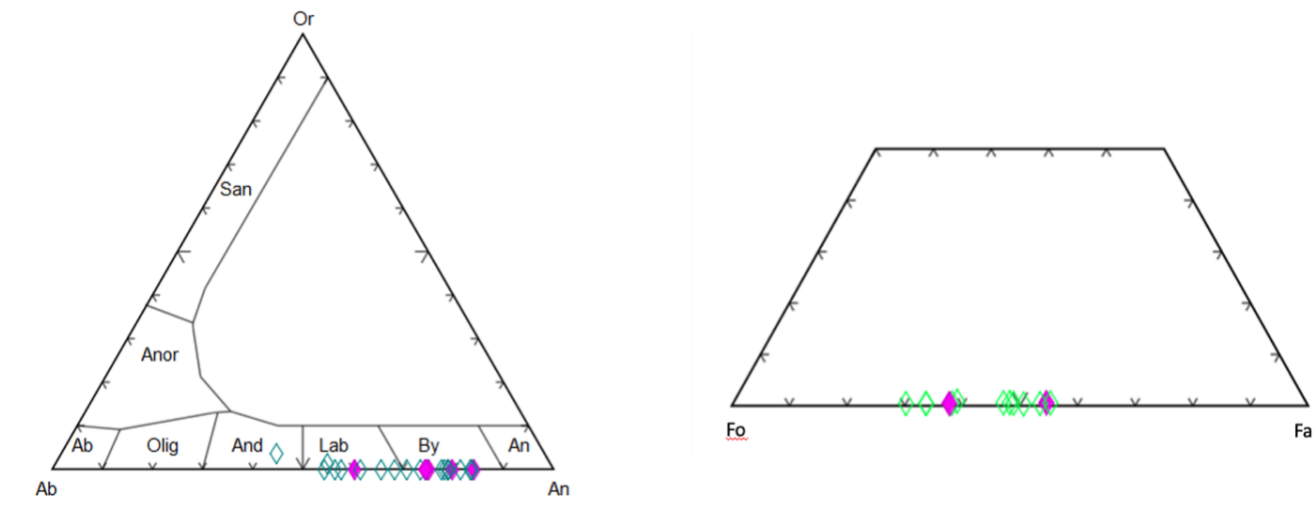

Figure 3.13 Left: Feldspar diagram with compositions from CSS-10. Cores are plotted as solid diamonds and rims are plotted as plotted as empty diamonds. Right: Olivine-pyroxene quad with compositions from CSS-10. Cores are plotted as solid diamonds and rims are plotted as plotted as empty diamonds.

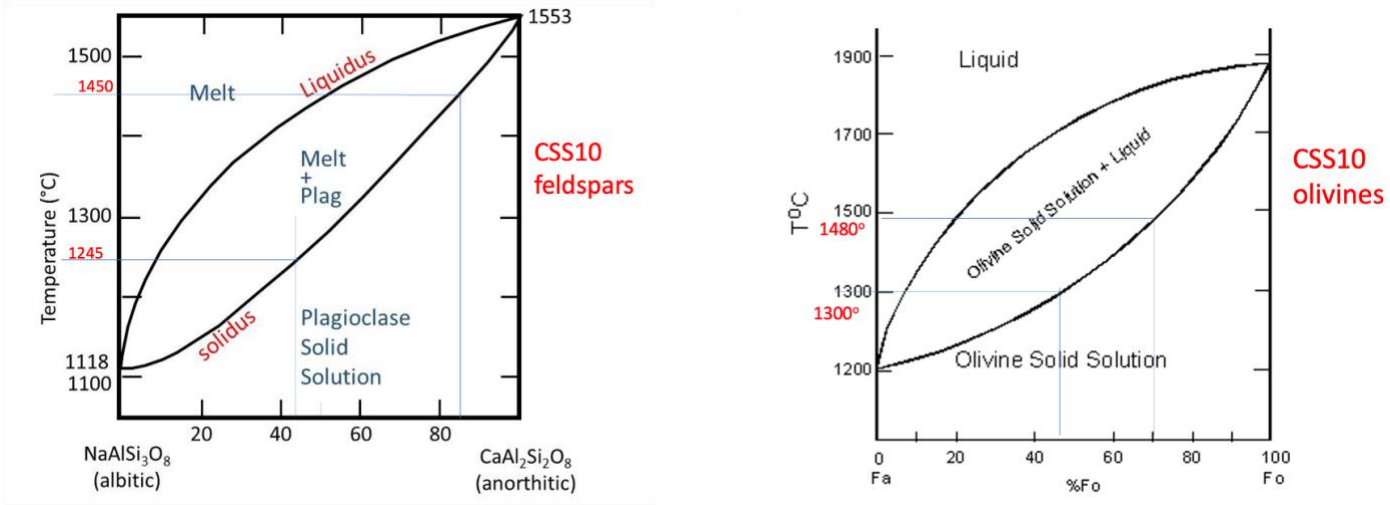

Figure 3.14 Left: A diagram of plagioclase feldspar solid solution with the end member compositions from CSS-10 plotted with their accompanying temperatures of formation. Right: A diagram of olivine solid solution with the CSS-10 compositions plotted showing the attributed temperatures of formation.

3.3.4 CSS-11

The compositions of three zoned plagioclase feldspars were taken and plotted on a ternary feldspar diagram (Figure 3.15). These feldspars showed compositions of $An_{55}Ab_{44}Or_1$ to $An_{82}Ab_{18}$. One zoned olivine composition was plotted on a pyroxene olivine quadrangle and

showed compositions between Fo_{56} to Fo_{64} (Figure 3.15). In Figure 3.16 these compositions were used to plot the average temperatures of formation of the feldspars and olivines. The feldspars plotted formation temperatures between 1300°C to 1435°C and the olivines plotted temperatures around 1360°C to 1430°C.

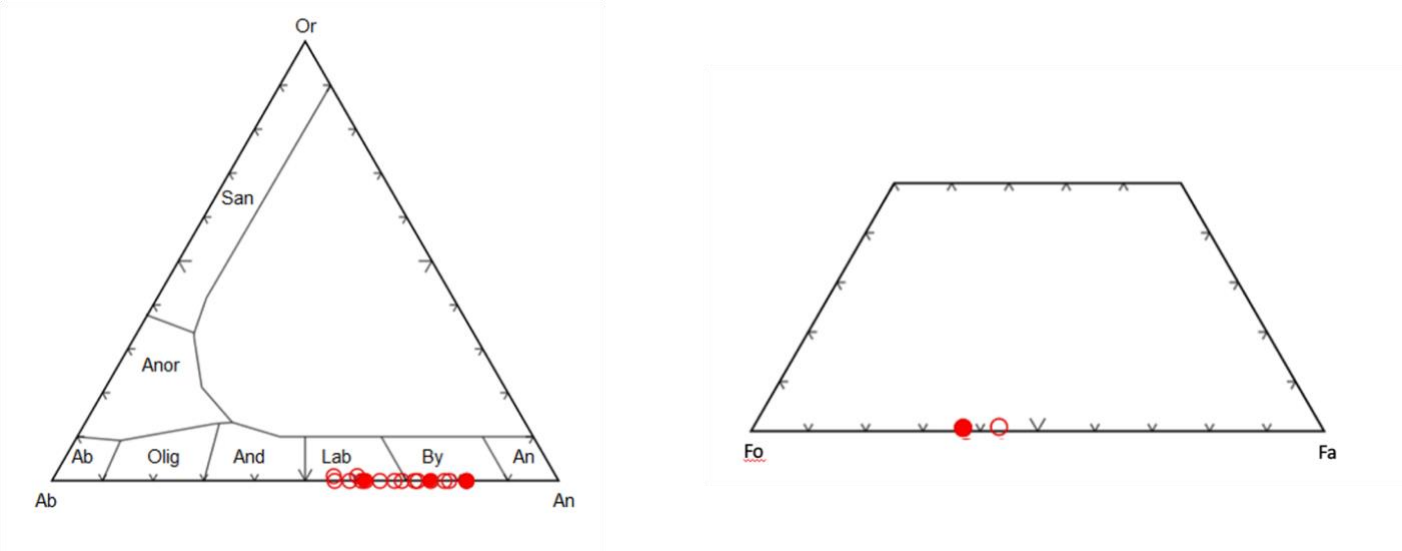

Figure 3.15 Left: Feldspar diagram with compositions from CSS-11. Cores are plotted as solid circles and rims are plotted as plotted as empty circles. Right: Olivine-pyroxene quad with compositions from CSS-11. Cores are plotted as solid circles and rims are plotted as plotted as empty circles.

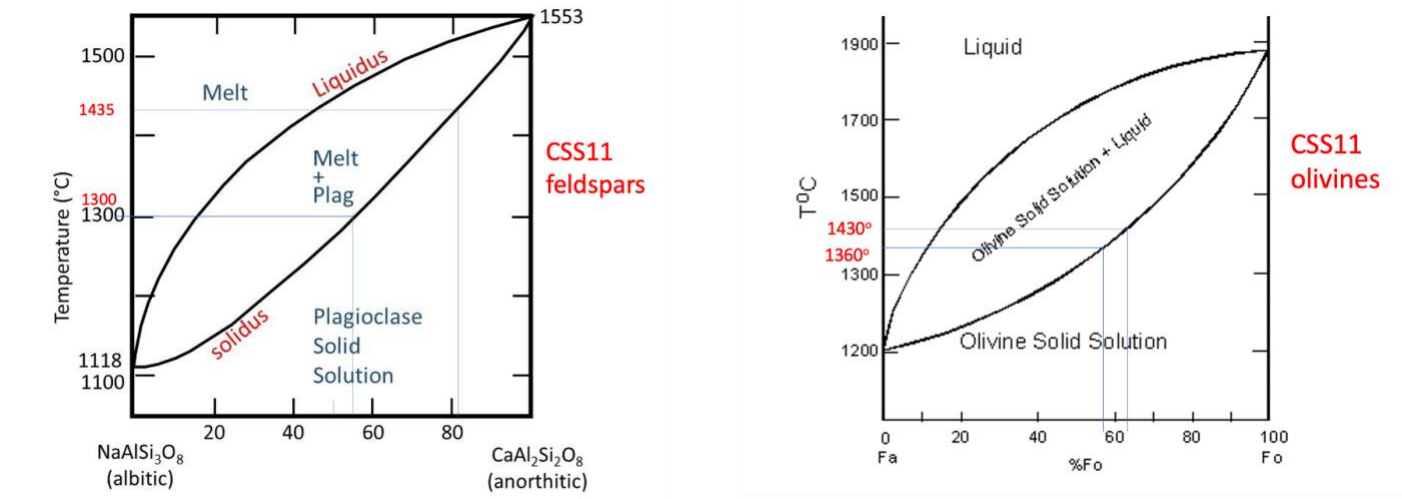

Figure 3.16 Left: A diagram of plagioclase feldspar solid solution with the end member compositions from CSS-11 plotted with their accompanying temperatures of formation. Right: A diagram of olivine solid solution with the CSS-11 compositions plotted showing the attributed temperatures of formation.

4. Discussion

4.1 Eruptive Episodes

Calc-Alkaline and tholeiitic basalts form in different ways. Tholeiitic basalts are formed shallower within the crust and reabsorb olivines crystallized early on. This results in these melts having an early enrichment in iron and magnesium. Calc-Alkaline basalts are formed deeper within the crust and are depleted in iron and magnesium earlier in the stages of crystallization, with minerals like olivines showing more zoning with fewer pyroxenes. The separation of CSS-10 and CSS-11 in Figure 3.2 as tholeiitic while the other upper CSS flows showed calc-alkaline affinities suggests that these flows formed from two different parent magmas that behaved according to these different basalt types. The presence of two different parent magmas would mean CSS-10 and CSS-11 were a part of a different eruptive period than the younger flows sitting on top of them.

In Figure 3.3, CSS-10 and CSS-11 stand apart from the younger CSS flows not only due to stratigraphic position, but because they are also more depleted in magnesium, iron, strontium, nickel, chromium than all the upper stratigraphy. This separation by composition indicates that these flows were not erupted during the same period as CSS-1 through CSS-9. CSS-10 and CSS-11 follow the same compositional trends as the lower CSS flows in strontium, nickel, and chromium but have significantly higher levels of magnesium. They could have been erupted at the same time as these older flows and represented the beginning of a change in the magma source however they could also have been a short intermediate composition eruption before the larger changes that we see between the lower flows and CSS-1 through CSS-9.

4.2 Primitivity

In Hildreth and Moorbath 1988, they assert that the Transitional Southern Volcanic Zone is home to very few primitive compositions. This paper also insists that the rock types located in the TSVZ mainly range between dacites and andesites. The whole rock geochemistry data analyzed from the Casitas Shield contradicts both claims. The rock type classification in Figure 3.1 shows that there are no compositions close to a dacite within the sampled CSS-CSN flows, and that they are instead trending more and more mafic over time. One of these flows plots fully as a basalt, while most of the upper CSS flows plot right on the line between basaltic andesites and basalts. These mafic compositions more accurately reflect mantle compositions and primitivity than the believed trend in dacitic and andesitic compositions that require more contamination by the continental crust and possible MASH zones.

The mantle is enriched in magnesium and iron and is composed of mostly olivines and pyroxenes. Figure 3.3 plots the elements that most directly indicate the primitivity of a melt, or the amount that a given flow reflects the composition of the mantle with little crustal contamination. The magma system becomes significantly enriched in magnesium and iron within the upper CSS flows. The entire system is depleting in strontium over time but has an overall very high ppm concentration. Strontium is a trace element that follows calcium which is present in higher quantities in mafic and primitive compositions due to the crystallization of orthopyroxenes. Nickel and chromium are key elements in the crystal structure of olivines, and their sudden increase in the upper CSS flows indicates a higher crystallization of olivines in these flows. Each individual plot within Figure 3.3 shows an increase in the primitivity of the magma within the Casitas Shield magma system over time.

Figure 3.4 looks more specifically at just the strontium and magnesium composition of the sampled Casitas Shield flows to the rest of the Southern Volcanic Zone. Despite their location in a region of the SVZ that Hildreth and Moorbath 1988 claims produces far fewer mafic or primitive compositions, the CSS-CSN magmas plot among the highest magnesium levels and have a significantly higher strontium content. Even though Figure 3.3 showed than strontium depleted within this system over time, these flows still indicate a higher primitivity than most of the other flows within the 1400km long SVZ. This is supported by the behavior of rubidium within the CSS-CSN samples, shown in Figure 3.5. Rubidium is a large ion lithophile element that is easily pulled into a magma during any contamination with country rock, and rubidium depletion indicates that there is a low level of crustal contamination in the flow. The CSS-CSN suite plots well under most of the SVZ, supporting the high primitivity of these flows as compared to the rest of the SVZ. While strontium is also a large ion lithophile, it behaves opposite from rubidium in these samples. This is another indicator of primitivity, meaning that the high amount of strontium present within the melt did not come from contact with the surrounding country rock, but instead followed the high levels of calcium present in minerals associated with melt primitivity.

4.3 Crystallization Temperatures and Dominant Petrogenetic Processes

The temperature range over which a flow must have crystallized can be determined by using both the temperatures of formation for the feldspars and olivines from each flow analyzed in thin section. CSS-1 crystallized between 1360°C and 1375°C. CSS-5 crystallized between 1300°C and 1475°C. CSS-10 crystallized between 1300°C and 1450°C. CSS-11 crystallized between 1360°C and 1430°C. The error in these temperatures is likely around 10°C, and they could have been better constrained by analyzing a greater number of feldspars or olivines in each sample.

The presence of normal zoning in plagioclase feldspar is a strong indicator of fractional crystallization, with the calcium core representing the composition of the magma system at the beginning of crystallization. As the magma cools sodium increasingly substitutes for calcium in forming subsequent rims on the feldspar. Normal zoning in the CSS-CSN, like that in Figure 3.6, indicates that these flows underwent some amount of fractional crystallization. However, a greater amount of oscillatory zoning was also seen, such as in Figures 3.7 and 3.8. During this type of zoning process, calcium and sodium alternate at different times during growth instead of simply increasing and decreasing during crystallization. Magma mixing or large-scale assimilation could be used to explain this change in composition. Magma mixing typically dominates in a subduction arc environment, with new melts replenishing the magma system at different times and introducing new end members. In the case of the Casitas Shield, this mixing could have been between the current present more primitive compositions and a dacite indicated by the early eruption of dacite at Cerro Azul during the modern eruptive period. Assimilation could also be a cause for oscillatory zoning, either in the form of overall system composition change or in the depositions of xenocrysts that remelt and begin to crystallize more rims. The composition change from assimilation could be attributed to rocks from nearby granitic plutons or underlying marine sediments.

The DGCA is similar in many ways to the Tatara-San Pedro volcanic complex (TSP) that lies just to the South. These complexes are the same age, experience the same crustal thickness and location within the TSVZ, and the TSP has a similar number of exposed lava flows in glacially eroded depressions in the topography studied in Dungan et al. 2001. These flows also produced primitive basalt compositions but ranged up to rhyolitic compositions as well. Comparing the data from flows within the DGCA to flows within the TSP can help to establish whether these

seemingly related volcanoes are behaving independently from one another, and how they compare to the arc as a whole. When the trace element data from the Casitas Shield is compared with trace element data from the TSP and the entirety of the SVZ published in Dungan et al. 2001, the CSS-CSN suite behaves similarly in most incompatibles aside from rubidium, zirconium, barium, and strontium. The Casitas Shield flows have a lower amount of rubidium, zirconium, and barium. However, these elements still seem to follow the same general trajectories as the TSP and the rest of the SVZ. The lower amount of LILEs and HFSEs within the Casitas Shield samples indicate a different degree of partial melting than seen in other parts of the SVZ and even in volcanic complexes nearby in the TSVZ. In the case of strontium, which is plotted in Figure 4.1, the Casitas Shield has higher concentrations that also behave oppositely from the concentrations found in the TSP and the trends from the SVZ. The difference in the behavior of strontium from other incompatibles like rubidium suggests that it doesn't come from partial melting, but instead from the assimilation of country rock that is enriched in calcium.

Overall, it is difficult to determine one single petrogenetic process due to the different eruptive episodes present between the CSS-CSN suite. The behavior of the whole system seems to have changed over time, shown in the production of more primitive magmas. It is likely that source related differences produced different parental magmas and this could be coupled with a change in the dominant petrogenetic process as well. Lavas from the upper CSS section of the Casitas Shield have high magnesium, nickel, and chromium which is unique compared to compositions throughout the TSVZ. The presence of these primitive magmas is further evidence of different parental sources. It is not likely that one process is entirely responsible for the petrogenesis of the suite, but that a combination of a small amount of assimilation-fractional

crystallization along with a more dominant presence of magma mixing contributed to the crystallization of the Casitas Shield flows.

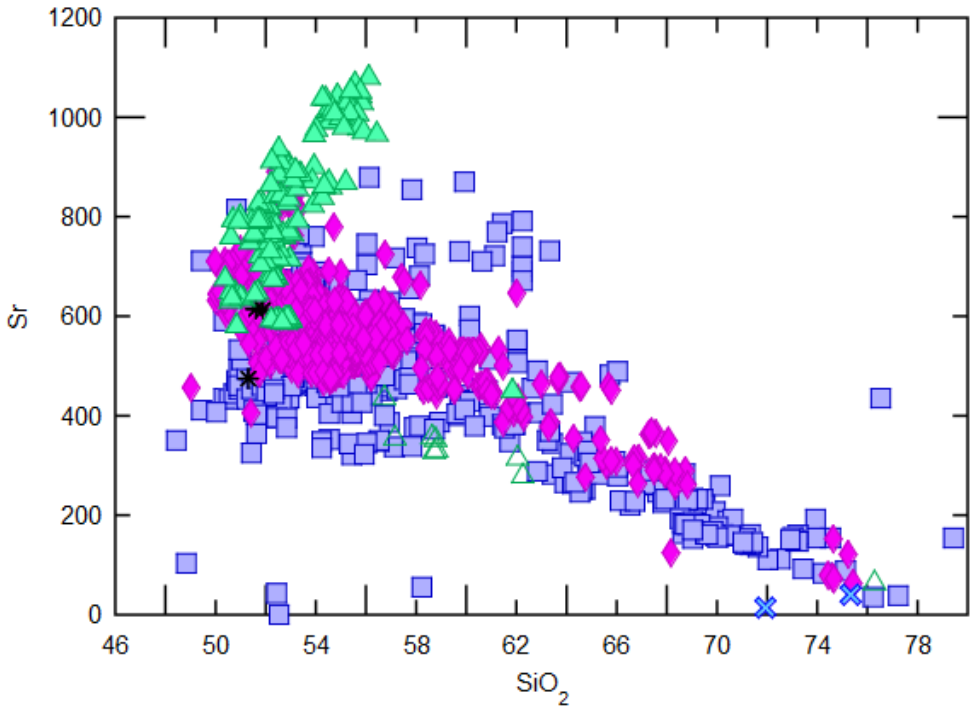

Figure 4.1 A plot showing the strontium of the Casitas Shield samples (green), Tatara-San Pedro samples (pink), and samples from the entire SVZ (purple). While the TSP has compositions of strontium that follow the entire broad range of strontium values in the SVZ, the CSS-CSN samples are more enriched in strontium and behave oppositely from the rest of the arc.

5. Conclusion

The primitive flow compositions found within the Casitas Shield beneath the Descabezado Grande-Cerro Azul volcanic complex contradict the findings in Hildreth and Moorbath, 1988 that claim the Transitional Southern Volcanic Zone lacks primitive basalts or mafic compositions. These findings suggest that the behavior of the Southern Volcanic Zone cannot be so easily narrowed down to section by section variation, and instead suggests that other components of the subduction arc factory combine to play a larger role in magma composition. Preliminary geochronologic dates for the Casitas Shield lie between 0.43 to 0.56 Ma. In order to better understand the other factors affecting the melts within the DGCA magmatic system, further work could be done analyzing isotopic ratios such as $^{87}Sr/^{86}Sr$ or $^{143}Nd/^{144}Nd$ to better understand the crustal contributions to the melt compositions. In addition, higher resolution geochronologic analyses would further constrain the eruptive interval of the Casitas Shield.

References

Bowen, N.L. (1922). The reaction principle in petrogenesis. Journal of Geology, v. 30, no. 4, p. 339-359.

Dungan, M.A., Wulff, A., and Thompson, R. (2001). Eruptive stratigraphy of Tatara-San Pedro complex, 36ºS, Southern Volcanic Zone, Chilean Andes: Reconstruction method and implications for magma evolution at long-lived arc volcanic centers. Journal of Petrology, v. 42, no. 3, p. 555-626.

Dungan, M. A., Davidson, J. (2004). Partial assimilative recycling of the mafic plutonic roots of arc volcanoes: An example from the Chilean Andes. Geology, 32.

Higgins, D. M., Voos, S., Auwera J. V. (2015). Magmatic processes under Quizapu volcano, Chile, identified from geochemical and textural studies. Contributions to Mineralogy and Petrology, 170.

Hildreth, W. & Drake, R.E. (1992). Volcán Quizapu, Chilean Andes. Bulletin of Volcanology, 54, 93–125.

Hildreth, W. & Moorbath, S. (1988). Crustal contributions to arc magmatism in the Andes of Central Chile. Contributions to Mineralogy and Petrology, 98.

Philpotts, A.R., and Ague, J.J. (2009). Principles of igneous and metamorphic petrology. Cambridge University Press.

Salas, P.A., Rabbia, O.M., Hernández, L.B. *et al.* (2017). Mafic monogenetic vents at the Descabezado Grande volcanic field (35.5°S–70.8°W): the northernmost evidence of regional primitive volcanism in the Southern Volcanic Zone of Chile. International Journal of Earth Sciences (Geol Rundsch), 106.

Salas, P., Ruprecht, P., Rabbia, O., Hernandez, L. (2021). Out-of-sequence skeletal growth causing oscillatory zoning in arc olivines. Nature Communications 12, 4069.

Stern, C.R. (2004). Active Andean volcanism: Its geologic and tectonic setting. Revista Geologica de Chile, 31.

Tormey, D.R., Mogk, D.W., and Manning, C.E. (1995). Mechanisms of crustal melting and melt extraction during regional metamorphism. Evidence from the Musgrave Block, central Australia: Geological Society of America Bulletin, v. 107, no. 4, p. 469-484.

Winslow, H. (2018). A study of Pleistocene volcano Manantial Pelado, Chile: Unique access to a long history of primitive magmas in the thickened crust of the Southern Andes. M.Sc. Thesis (unpubl.), University of Nevada, Reno.

Winslow, H., Ruprecht, P., Stelten, M. E., Amigo, A. (2020). Evidence for primitive magma storage and eruption following prolonged equilibration in thickened crust. Bulletin of Volcanology, 82.

Appendix: Major and Trace Element XRF Data

Sample	SiO2	TiO2	Al2O3	Fe2O3	MnO	MgO	CaO	Na2O	K2O	P2O5
CSN-1	55.36	0.8	18.44	7.61	0.13	4.28	7.69	4.12	1.33	0.3
CSN-2	55.87	0.82	17.72	7.39	0.12	5.21	7.28	4.23	1.25	0.3
CSN-3	55.68	0.82	17.63	7.39	0.12	5.34	7.26	4.14	1.24	0.3
CSN-4	55.33	0.8	17.58	7.52	0.13	5.33	7.67	4.02	1.21	0.29
CSN-5	55.63	0.81	17.73	7.56	0.12	5.22	7.47	4.07	1.25	0.29
CSN-6	54.63	0.86	17.55	7.73	0.13	5.46	7.91	3.87	1.27	0.28
CSN-7	55.74	0.8	18.29	7.35	0.12	4.61	7.46	4.06	1.35	0.3
CSN-8	55.53	0.77	18.22	7.31	0.12	4.51	7.52	4.04	1.35	0.29
CSN-9	56.08	0.75	18.28	7.26	0.13	4.21	7.41	4.16	1.33	0.3
CSN-10	55.24	0.84	17.98	7.51	0.13	4.79	7.72	4.09	1.3	0.29
CSN-11	55.34	0.76	18.75	7.53	0.13	3.92	7.72	4.02	1.35	0.3
CSN-12	55.17	0.76	18.73	7.46	0.13	3.96	7.74	4.09	1.32	0.3
CSN-12	55.28	0.77	18.71	7.52	0.13	3.95	7.69	4.15	1.34	0.3
CSN-14	55.81	0.72	18.86	7.52	0.14	3.56	7.57	4.03	1.36	0.3
CSN-15	55.75	0.74	18.89	7.49	0.13	3.58	7.58	3.86	1.35	0.3
CSN-16	54.93	0.81	18.81	7.79	0.14	3.84	7.8	3.95	1.29	0.29
CSN-17	55.39	0.8	18.97	7.78	0.13	3.72	7.71	4.11	1.31	0.29
CSN-18	55.22	0.82	18.93	7.83	0.14	3.82	7.83	3.79	1.28	0.29
CSN-19	53.32	0.97	19.31	8.41	0.14	4.24	8.35	4.07	1.11	0.23
CSN-20	52.49	0.99	19.76	8.6	0.14	4.36	8.51	4.09	0.99	0.22
CSN-21	52.99	0.97	19.48	8.42	0.14	4.25	8.43	4.01	1.08	0.23

CSN-22	52.84	0.99	19.53	8.53	0.14	4.27	8.47	3.81	1.06	0.23
CSN-23	52.88	0.97	19.53	8.38	0.14	4.31	8.45	4.09	1.08	0.23
CSN-24	53.9	0.94	19.17	8.48	0.14	3.96	7.96	4.18	1.16	0.25
CSN-25	52.56	1.07	19.12	8.86	0.14	4.39	8.45	3.86	1.03	0.23
CSN-26	52.7	1.08	19.22	8.93	0.15	4.37	8.44	4.15	1.02	0.22
CSN-27	52.59	1.09	19.11	8.98	0.14	4.4	8.47	4.09	1.02	0.22
CSN-28	52.31	1.11	19.23	8.98	0.14	4.55	8.65	4.05	0.98	0.21
CSN-29	51.68	1.13	19.08	9.24	0.15	4.75	8.72	4.06	0.93	0.21
CSN-30	51.86	1.11	19.06	9.03	0.15	4.65	8.79	3.79	0.93	0.21
CSN-31	52.1	1.13	19.17	9.09	0.15	4.67	8.79	3.83	0.92	0.21
CSN-32	52.13	1.12	19.13	9.06	0.15	4.59	8.79	4.11	0.94	0.21
CSN-33	52.11	1.14	19.08	9.12	0.15	4.59	8.74	3.86	0.95	0.21
CSN-34	54.27	0.94	18.87	8.21	0.15	3.87	7.91	4.31	1.19	0.26
Dike-1	51.56	0.68	14.98	8.58	0.15	11.68	8.67	2.49	0.69	0.18
Dike-2	51.84	0.68	14.95	8.49	0.15	11.39	8.83	2.68	0.75	0.17
Dike-3	52.21	1	17.14	8.91	0.15	7.49	7.99	3.54	1.03	0.23
Float	54.04	0.84	17.55	8.06	0.14	5.45	9.36	3.48	1.05	0.18
Hornitos Ejecta	51.26	0.65	14.15	8.78	0.16	12.44	9.03	2.19	0.7	0.13
CSS-1	52.2	1.07	18.42	8.78	0.14	5.95	8.56	3.87	0.91	0.25
CSS-2	52.93	1.05	18.01	8.63	0.14	5.79	8.28	3.8	1.07	0.25
CSS-3	51.95	1.05	17.96	8.87	0.14	6.58	8.29	3.58	1.04	0.24
CSS-4	52.15	1.04	17.9	8.92	0.14	6.66	8.41	3.7	0.99	0.24
CSS-5	52.41	1.01	17.69	8.81	0.14	6.58	8.33	3.74	1.01	0.24

CSS-6	52.35	1.01	17.76	8.94	0.15	6.61	8.24	3.72	1	0.22
CSS-7	52.29	1.01	17.76	9.01	0.14	6.76	8.21	3.75	0.99	0.23
CSS-8	52.1	1	17.55	9.07	0.15	6.97	8.16	3.35	0.98	0.21
CSS-9	52.19	1.02	17.63	9.2	0.15	7.07	8.17	3.71	1	0.23
CSS-9L	52.26	0.98	17.63	8.99	0.15	6.92	8.21	3.35	0.99	0.23
CSS-10	50.56	1.09	18.85	9.49	0.16	6.14	9.4	3.59	0.71	0.24
CSS-11	50.62	1.08	18.82	9.42	0.16	5.91	9.38	3.58	0.72	0.24
CSS-13	52.52	1.08	19.23	8.71	0.14	4.38	8.62	4.09	1.07	0.25
CSS-14	52.49	1.06	19.09	8.71	0.15	4.69	8.58	4.21	1.07	0.26
CSS-15	51.97	1.08	19.43	8.9	0.15	4.37	8.68	3.82	0.98	0.24
CSS-18	52.16	1.08	19.37	8.98	0.15	4.27	8.69	3.74	0.95	0.23
CSS-21	52.37	1.02	19.22	8.71	0.15	4.3	8.6	3.8	0.97	0.23

Table A1 Major oxide data fro the CSS-CSN suite of flows. Data is listed in wt %.

Sample	Nb	Zr	Sr	Zn	Ni	Cr	V	Ce	Ba	La	Y	U	Rb	Th	Pb
CSN-1	3.9	82	1054	69	24	16	150	36	415	18	14.4	2	27.3	3	12
CSN-2	3.5	69	972	68	55	73	131	32	421	16	12.7	2	21.7	2	11
CSN-3	3.2	68	979	63	56	75	120	32	427	15	12.8	1	22.2	2	10
CSN-4	2.9	61	1010	63	49	61	140	31	408	16	13.7	1	20.2	2	9
CSN-5	2.9	63	1008	63	47	56	129	32	403	14	13.9	2	21.1	3	9
CSN-6	3.4	73	1018	65	58	59	154	35	391	16	14.7	1	25.2	3	7
CSN-7	3.6	79	1053	67	45	39	143	37	431	18	14.5	2	26.4	3	10
CSN-8	3.4	77	1068	67	44	40	140	37	417	20	14.9	2	26.6	2	7
CSN-9	3.8	76	1081	74	30	25	140	37	425	17	14	3	24.9	3	11
CSN-10	3.8	75	1015	72	44	41	138	36	412	17	14.6	1	25.1	4	11
CSN-11	3.7	95	1030	72	18	9	147	36	429	20	15	2	28.3	4	10
CSN-12	3.6	91	1034	69	19	9	140	36	430	19	14.5	2	27.3	4	11
CSN-12	3.9	93	1034	72	19	8	150	38	427	18	14	2	27.4	3	9
CSN-14	3.8	99	1030	75	14	2	137	40	421	20	14.9	1	28.8	4	11
CSN-15	3.8	111	1044	74	11	3	133	37	429	15	15.1	2	28.1	3	11
CSN-16	4	102	1000	71	12	1	150	34	408	16	15.8	0	24.8	4	8
CSN-17	3.5	106	1002	67	14	2	143	36	411	16	15.5	2	26.4	4	8
CSN-18	3.8	103	995	67	10	1	143	29	413	18	16.1	2	25.7	4	8
CSN-19	2.8	80	887	76	16	5	203	26	316	15	16.3	2	19.9	2	7
CSN-20	3.2	84	937	74	14	3	195	27	340	10	16.4	1	15.3	2	7
CSN-21	2.9	82	896	73	15	4	199	29	326	12	16.4	1	18.5	2	8
CSN-22	2.8	84	903	71	16	2	200	29	346	14	16.5	0	18.2	2	7

CSN-23	3	82	907	71	14	2	193	28	345	15	16.9	1	18	3	9
CSN-24	2.8	85	902	72	15	1	180	30	349	16	16.2	2	21.1	3	8
CSN-25	3.2	80	845	67	14	3	188	29	315	12	17.1	1	17.2	2	5
CSN-26	3.1	75	842	66	13	4	174	23	332	11	17.3	0	15.8	2	6
CSN-27	2.7	80	848	64	15	5	167	27	326	14	17.2	1	16.5	3	7
CSN-28	3.4	80	842	65	16	9	224	26	317	14	17.3	1	15.3	3	5
CSN-29	3.3	78	828	67	19	9	193	25	322	12	17.6	1	11.4	1	7
CSN-30	2.5	78	826	66	15	8	187	24	308	9	17.8	1	12.7	2	7
CSN-31	2.7	75	822	69	15	10	217	23	297	11	18.1	1	11.5	1	8
CSN-32	2.9	73	817	65	18	7	200	24	309	12	17.8	1	13.1	2	5
CSN-33	2.8	73	801	65	15	9	200	24	308	12	17.9	1	13.8	1	5
CSN-34	3.3	90	861	69	14	8	159	31	363	15	16.1	2	19.5	3	9
Dike-1	2.3	53	617	77	226	775	187	16	219	9	12.3	1	11.1	1	6
Dike-2	1.9	58	615	75	207	761	187	20	203	10	12.2	2	11.7	2	7
Dike-3	2.6	82	659	81	101	199	189	24	309	13	15.2	2	20.3	2	7
Float	3.1	74	687	79	21	103	218	21	268	12	12.9	2	22.8	3	12
Hornitos Ejecta	1.1	55	477	78	279	1069	203	17	175	7	13	3	15.5	2	9
CSS-1	3.7	85	712	80	55	104	206	29	359	12	16.2	1	7.9	2	9
CSS-2	3.7	95	716	77	51	99	186	27	350	12	15.6	2	18.8	2	5
CSS-3	3.6	94	726	79	78	139	191	33	348	14	16.4	2	15.5	2	7
CSS-4	3.9	96	708	82	74	149	205	28	325	14	17.1	2	16.4	2	8
CSS-5	3.8	91	679	77	74	168	196	24	316	13	16.8	2	17	2	6
CSS-6	3.6	89	681	77	85	227	182	29	322	12	15.8	2	17	1	6

CSS-7	3.6	88	688	75	87	201	172	24	336	16	15.3	1	17.3	3	5
CSS-8	3.9	87	684	76	97	213	166	25	323	14	15.6	2	17.3	2	5
CSS-9	3.6	88	683	73	86	180	161	29	327	11	16.1	2	16.5	2	8
CSS-9L	3.6	86	675	83	106	266	200	26	309	12	16	1	17.7	2	8
CSS-10	3.3	97	650	77	45	77	223	28	282	9	17.7	1	8.8	2	6
CSS-11	3.8	94	638	79	54	78	219	27	285	9	18	1	8	2	6
CSS-13	3.4	98	722	66	21	29	181	26	335	11	19.1	1	19.3	2	6
CSS-14	3.9	99	734	73	22	35	208	29	345	16	20.1	1	15.6	1	8
CSS-15	3.5	98	717	69	26	36	185	33	342	14	19.9	1	18.5	1	7
CSS-18	3.8	98	711	65	20	30	176	29	351	12	19.9	2	18.8	1	9
CSS-21	3.4	106	705	78	27	41	209	29	340	13	21.3	2	12.7	2	9

Table A2 Trace element data from the CSS-CSN suite in parts per million..